

We are IntechOpen, the world's leading publisher of Open Access books Built by scientists, for scientists

6,900

Open access books available

185,000

International authors and editors

200M

Downloads

Our authors are among the

154

Countries delivered to

TOP 1%

most cited scientists

12.2%

Contributors from top 500 universities



WEB OF SCIENCE™

Selection of our books indexed in the Book Citation Index
in Web of Science™ Core Collection (BKCI)

Interested in publishing with us?
Contact book.department@intechopen.com

Numbers displayed above are based on latest data collected.
For more information visit www.intechopen.com



Technological Challenges for Efficient AlGaAs Nonlinear Sources on Chip

M. Savanier, C. Ozanam, F. Ghiglieno, L. Lanco,
X. Lafosse, A. Lemaître, I. Favero, S. Ducci and G. Leo

Additional information is available at the end of the chapter

<http://dx.doi.org/10.5772/52201>

1. Introduction

Photonics puts at stake a wide variety of applications, from applied fields of physics, such as ultrafast all-optical signal processing [1] or pollutant monitoring [2], to more fundamental ones, *e.g.* quantum information [3], and its convergence with electronics at chip-scale level is one of today's great scientific and technological challenges. As a consequence, the full integration of optoelectronics devices on existing developed platforms is expected to be the next technological leap, with major breakthroughs in telecommunications, industry and health. While the main building blocks of optical integrated circuitry have been reported in the standard SOI platform [4], coherent light sources still markedly lack to achieve this transition of paradigm. To date, the hybrid conjunction of silicon photonics and direct-gap III-V compounds appears to be one of the most promising key technologies towards large-scale photonic integration and scalability [5]. In particular, such photonics platform could capitalize advanced functionalities enabled by guided-wave quadratic nonlinear optics. Thus, the demonstration of the electrically pumped versions of an optical parametric oscillator (OPO) or of a telecom twin-photon source (TTPS) would have a great impact on applications requiring room-temperature operation and wide tunability.

In this context, the Aluminum Gallium Arsenide (AlGaAs) system is an ideal candidate for the nonlinear photonic design, because of its numerous advantages: high second order susceptibility, wide transparency window, good thermal conductivity and monolithic integration.

In order to design efficient frequency converters, the key issue is to keep a constant phase relation between the three interacting waves. In general, this is not a trivial task because of the phase-velocity mismatch induced by the material chromatic dispersion [6]. While few phase-

matching strategies have been investigated, an original modal phase-matching scheme based on Bragg reflector waveguides has been recently addressed, reviving the interest for spontaneous parametric down-conversion (SPDC) in AlGaAs-based waveguides [7,8].

In this chapter we will focus on AlGaAs-based nonlinear waveguides in which phase-matching is achieved through form birefringence, artificially induced in optical heterostructures by selective oxidation of Al-rich layers into Aluminum Oxide (referred to as AlOx thereafter). Despite recent technological improvement and promising performances for frequency conversion in the near [9] and mid-infrared regions [10], neither the OPO nor the TTPS has been demonstrated yet on chip, because of technological issues, mainly excessive propagation losses and absence of appropriate built-in cavity. In the second section we present the scientific context of this work, focusing on AlGaAs integrated nonlinear devices exploiting the so-called form birefringence phase-matching scheme. Section three is devoted to the design procedure and the optimization of the fabrication process of two types of partially oxidized waveguides, while their experimental performances are summarized in section four. A comprehensive study of the different loss mechanisms involved is presented in section five, and the design and fabrication of built-in cavity mirrors is described in the sixth section.

2. Integrated frequency converters in the infrared

2.1. Key importance of the near and mid-infrared ranges

Near and mid-infrared radiation corresponds to the region of the electromagnetic spectrum with wavelengths spanning between 1 and 20 μm . It contains two telecom windows (around 1.3 and 1.5 μm) as well as strong characteristic roto-vibrational lines of many molecules (pollutants, toxins, etc.) and two atmospheric transmission windows (3-5 μm and 8-13 μm), which makes it essential for civilian and military applications such as spectroscopy, material processing, molecular sensing, thermal imaging and defense.

The current state-of-the-art sources developed for these applications can be categorized in three main groups: solid-state and fiber lasers, semiconductor lasers, and parametric sources. Although the former include a wide variety of well-known and established emitters, they still remain macroscopic objects falling out of the scope of on-chip integration, and their tunability is severely limited by the discrete energy transitions of the active media [11]. On the contrary, since their first demonstration respectively 50 and almost 20 years ago [12,13], laser diodes and quantum cascade lasers (QCLs) have greatly benefited from the flexibility enabled by the engineering of energy band structure and from clean-room fabrication technologies. Yet, these two technological streams hardly overlap in the wavelength range around 3 μm . So far, room temperature operation has only been demonstrated for III-V antimonide laser diodes operating in continuous-wave (CW) regime up to 3.0 μm [14]; and for QCLs (either grown on InP substrate or in the III-V antimonide system) with emission wavelength extended down to 3.1 μm in pulsed regime, and to 3.6 μm CW [15,16]. However, because of its controllability and re-growth constraints, commercial producers tend to avoid the use of antimony. That is why antimonide laser diodes are not yet standard

off-the-shelf products, whereas QCLs, thanks to a mature and possibly Sb-free technology, are now finding commercial applications and increasingly replace the outdated lead-salt laser diodes. Nevertheless, integrated semiconductor sources are still lacking around 3 μm , and apart from few QCL products (*e.g.* $\lambda \sim 3.3 \mu\text{m}$ by Daylight Solutions), solid state and nonlinear optics-based sources represent the majority of commercially available sources [17]. Recently, intra-cavity second harmonic generation (SHG) has been reported in QCLs, extending their emission range to wavelengths as small as 2.7 μm , at the price of poor conversion efficiency though [18].

Nonlinear optics, by means of difference frequency generation (DFG) and optical parametric oscillation, is a well-known alternative to cover the whole 1-10 μm span. The wide variety of spectral/temporal formats allowed by nonlinear $\chi^{(2)}$ processes in transparent materials, endows parametric sources with a high level of flexibility. Moreover, SPDC is currently the most widely used process to generate quantum photon pairs, which have become one of the building blocks of quantum information. To date, room-temperature SPDC has been reported in passive AlGaAs waveguides designed to perform 0.775-to-1.55 μm down-conversion [7,8], while entanglement has been demonstrated in light emitting diodes only at cryogenic temperature [19]. Thus, the fabrication of an electrically-pumped version of such light source operating at room temperature in the telecom range also constitutes a high-potential and challenging goal.

2.2. Integration of nonlinear devices

Fulfilling the phase-matching condition is crucial for efficient three-wave mixing. The classical approach to cancel out the phase-velocity mismatch between the interacting waves is to rely on the birefringence of the nonlinear medium. The limited choice of suitable materials led to quasi-phase matching (QPM), well established in ferroelectric crystals, with a great impact on the fabrication of infrared parametric sources. QPM consists in a periodic inversion of nonlinearity along the propagation direction, minimizing the phase-mismatch to allow the nonlinear interaction to build constructively. In this context, the development of bulk dielectric crystals like periodically-poled LiNbO₃ (PPLN) has made them the workhorse materials of $\chi^{(2)}$ optics. Besides, by implementing a guided-wave configuration in which the three optical modes are confined and can interact over several centimeters, normalized conversion efficiencies up to $\sim 150 \text{ \%W}^{-1}\text{cm}^{-2}$ have been demonstrated [20], yielding to the demonstration of compact and efficient photon pairs sources [21] and OPOs [22]. Nonetheless, such setups are composed of discrete optical components with critical alignment and do not lend themselves to optoelectronic integration. That is why direct-gap semiconductor compounds, provided that they have significant second-order nonlinearity, are an attractive platform for the coming years' photonics, thanks to mature nano-fabrication technology. Indeed they promise on-chip integration of both efficient frequency converters and laser pumps. Gallium arsenide (GaAs), or more generally the AlGaAs system, is particularly interesting because it exhibits a huge second-order nonlinearity ($d_{14} \sim 100 \text{ pm/V}$), a broad transparency window (from 0.9 to 17 μm), and a large variety of design and fabrication solutions [23]. Because AlGaAs is neither birefringent nor ferroelectric, phase matching

is not a trivial task, especially if the frequencies involved lie close to the material bandgap, where the dispersion is strong. Similarly to lithium niobate, the demonstration of QPM in bulk orientation-patterned GaAs (OP-GaAs) [24] enabled the demonstration of efficient tunable infrared sources, including the first GaAs-based OPO in 2004 [25]. Regarding OP-GaAs waveguides, in addition to their complex fabrication process, their performances are limited by high optical losses due to scattering in the corrugated waveguide core, resulting in modest normalized conversion efficiencies of $\sim 90 \text{ \%W}^{-1}\text{cm}^{-2}$ [24]. Another approach, based on the engineering of modal dispersion, enabled the implementation of two additional phase-matching strategies:

1. modal phase-matching, involving transverse modes of different order at the price of a worse nonlinear overlap integral [8]; and
2. form-birefringent phase matching.

The latter relies on optical heterostructures, in which thin low-index non-stoichiometric AlOx layers are intertwined with AlGaAs layers, so to artificially induce the necessary birefringence to compensate for the chromatic dispersion [10]. For these two schemes, normalized conversion efficiencies of $\sim 250 \text{ \%W}^{-1}\text{cm}^{-2}$ and $\sim 1000 \text{ \%W}^{-1}\text{cm}^{-2}$ have been reported respectively, confirming that nonlinear integrated GaAs-based devices are a credible and promising alternative to standard LiNbO₃.

2.3. Form birefringence phase matching scheme

Since AlGaAs is optically isotropic, the standard birefringent phase-matching scheme cannot be implemented. Nevertheless, in a guided-wave configuration, a small anisotropy appears as the TE₀₀ and TM₀₀ solutions of the Maxwell equations experience different boundary conditions, hence leading to a non-zero birefringence $|n(\text{TE}_{00}) - n(\text{TM}_{00})|$. The latter can then be tailored for fundamental, orthogonally polarized eigen modes. However this quantity is in general much smaller than the dispersion, so that this technique remains unsuitable to phase match any nonlinear interaction.

In order to boost this effect and artificially induce a significant amount of birefringence, one can pattern the waveguide core at sub-wavelength scale, by repeatedly breaking the refractive index continuity with a two-material multilayer. The resulting metamaterial behaves as a macroscopic uniaxial crystal, whose birefringence is fully determined by the index contrast and the filling factors of the materials [27]. In particular, this so-called form birefringence phase-matching scheme has been developed in the AlGaAs platform during the late 90's at Thomson CSF laboratory (today Alcatel Thales III-V Lab) [26]. Thanks to the wide variety of index profile designs enabled by the dependence of refractive index with the aluminum fraction, the phase-matching condition can be engineered at will.

The first phase-matched interaction of this type dates back to the seventies, with the doubling of a CO₂ laser emitting at 10.6 μm [27]. In that case, given the weak material dispersion in the mid-infrared (few 10^{-2}) an AlAs/GaAs heterostructure suffices to meet the phase-matching condition. However, since the material dispersion strongly increases when the frequencies of the interacting waves lie close to the bandgap of the material, nonlinear

interactions between the visible and the mid-infrared are then prevented for the simple Al-GaAs platform.

In 1990, the discovery of selective wet oxidation of Al-rich AlGaAs layers drastically broadened the potential of form-birefringent phase-matching, thanks to the density, homogeneity and stability of a new type of aluminum oxide [28]. This material exhibits nice optical properties, such as a wide transparency window and a low refractive index of ~ 1.6 , and is electrically insulating. A few engineering domains rapidly took advantage of these physical properties: electronics, with field effect transistors [29]; optics, with broadband Bragg mirrors [30]; and optoelectronics, by combining optical and electrical confinement in vertical-cavity surface-emitting lasers (VCSELs) to improve their yield and ensure single-mode emission [31].

In the case dealt with in this chapter, the GaAs/AlO_x system allows accessing birefringence of several 10^{-1} , *i.e.* up to one order of magnitude higher than in a GaAs/AlAs heterostructure. This in turn enables to phase-match any nonlinear quadratic interaction with wavelengths spanning from the visible to the mid-infrared region [9,10,32]. Despite this substantial advantage, this material is not yet completely mature for demanding photonics applications, and its fine understanding is a matter at the intersection of photonics and materials science.

3. Design and fabrication of the devices

3.1. Design guidelines of partially oxidized AlGaAs waveguides

To demonstrate the high potential of the form birefringence phase-matching scheme, we have implemented it into two multi-layered structures designed for the down-conversion of pumps with respective wavelength $1.06\ \mu\text{m}$ and $0.775\ \mu\text{m}$. The first device is intended to perform as an OPO in the near and mid-infrared regions, while the second one is meant to operate as a TTPS.

For each structure, the design's objective is to balance the combined material and waveguide dispersions with enough induced birefringence, taking into account the following criteria:

- the transverse dimensions of the waveguide should favor zero-order modes to maximize their nonlinear overlap integral and avoid injecting power into non phase-matched higher order modes,
- the aluminum fraction in the guiding core should be low to optimally exploit the $\chi^{(2)}$ nonlinearity of the material, which must also be transparent at every frequency involved in the three-wave mixing,
- the aluminum fraction in the claddings should be high enough for a good confinement of the waves, but also guarantee the stability of the material, with no parasitic spontaneous oxidation,
- the number of AlO_x layers should be kept as small as possible as their second order susceptibility is zero and their quality is expected to be worse than crystalline lattice-matched AlGaAs.

Moreover, our choice is for type I phase-matching, rather than type II, as it requires a smaller amount of birefringence (and therefore of AlOx). According to this configuration and the non-zero elements of the second order susceptibility tensor of GaAs, quadratic interactions are only possible between a combination of two low frequency TE modes (*i.e.* with polarization in the layers plane) and a higher frequency TM mode (*i.e.* with polarization perpendicular to the layers plane).

For technological reasons, the thickness of the Al-rich layers to be oxidized must be comprised between few nanometers and few microns. Indeed, the diffusion of oxidant species along very thin layers is impeded, and the overall mechanical stability of thick oxidized layers is critical. However, this mechanical instability can be mitigated by adding a small amount of gallium to the thin AlAs layers [33]. As a result, we have chosen to deal with ~30 nm layers of Al_{0.98}Ga_{0.02}As (basically AlAs). Note that all the thicknesses of the oxidized layers are fixed to be the same throughout the whole structure, so to optimally calibrate the oxidation process and benefit from the best experimental conditions.

While for the first “OPO structure”, the fulfillment of the phase-matching condition requires the insertion of only five AlOx layers in the GaAs core, the situation differs in two aspects for the “TTPS structure”:

- 1. the guiding core material must be switched to Al_{0.25}Ga_{0.75}As to ensure its transparency at 0.775 μm, and
- 2. due to the higher dispersion generated by the proximity of the material bandgap, the number of AlOx layers must be significantly increased, leading to their insertion into the waveguide claddings as well.

In both cases, the thickness of the (Al)GaAs layers surrounded by oxide layers is set to tune the degeneracy wavelength. The two final designs are given in Tables 1 and 2, whereas the corresponding refractive index profiles and the intensity distributions of the phase-matched modes at degeneracy are shown in Figures 1 and 2.

Layer	Composition	Thickness (nm)	Repetition
Cap	GaAs	30	
Cladding	Al _{0.7} Ga _{0.3} As	1000	
Core	Al _{0.98} Ga _{0.02} As	37.5	× 4
	GaAs	273	
	Al _{0.98} Ga _{0.02} As	37.5	
	Al _{0.98} Ga _{0.02} As	37.5	
Cladding	Al _{0.7} Ga _{0.3} As	1000	
Buffer	Al _{0.92} Ga _{0.08} As	1000	
Substrate	GaAs	-	

Table 1. Multilayer sequence for 1.06 μm to 2.12 μm frequency conversion.

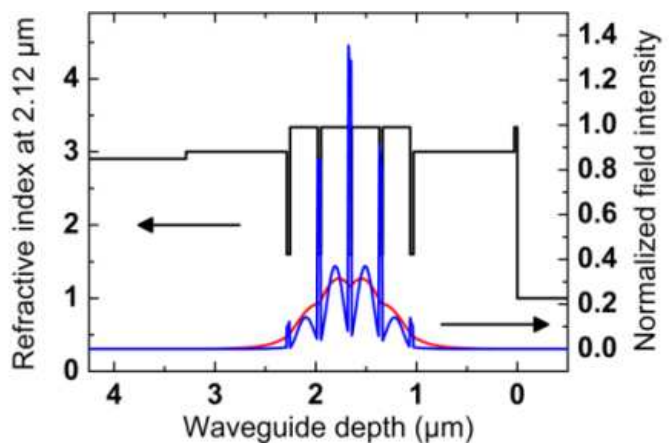


Figure 1. Refractive index profile (black line), phase-matched TE₀ (red line), and TM₀ (blue line) modes at 2.12 μm and 1.06 μm respectively, represented along the growth direction.

Layer	Composition	Thickness (nm)	Repetition
Cap	GaAs	30	
Cladding	Al _{0.8} Ga _{0.2} As	166	× 4
	Al _{0.98} Ga _{0.02} As	37.5	
Core	Al _{0.25} Ga _{0.75} As	166	× 8
	Al _{0.98} Ga _{0.02} As	37.5	
Cladding	Al _{0.8} Ga _{0.2} As	166	× 4
	Al _{0.98} Ga _{0.02} As	37.5	
Buffer	Al _{0.8} Ga _{0.2} As	100	
Substrate	GaAs	-	

Table 2. Multilayer sequence for 0.775 μm to 1.55 μm frequency conversion.

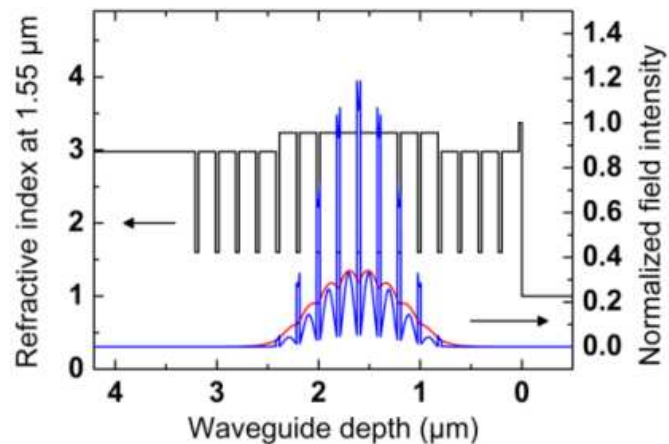


Figure 2. Refractive index profile (black line), phase-matched TE₀ (red line), and TM₀ (blue line) modes at 1.55 μm and 0.775 μm respectively, represented along the growth direction.

3.2. Waveguide fabrication steps

The main advantage of the form birefringence phase-matching scheme with respect to competing techniques is the inherently high nonlinear overlap integral between very look-alike fundamental modes. Thereby, nonlinear partially oxidized AlGaAs waveguides are expected to give interestingly high conversion efficiencies. However, their performances rely on the quality of their fabrication, for optical propagation losses heavily affect the phase-matching.

Fabrication improvements

Thanks to the well-developed clean-room techniques and equipments (*e.g.* epitaxial growth, lithography and cleaving) the AlGaAs platform is readily mature and compatible with the fabrication of high quality integrated devices. Furthermore, over the last fifteen years GaAs/AlOx waveguides have significantly benefited from the efforts and technological improvements achieved in terms of etching and oxidation [34].

The first mid-infrared DFG results have been reported in RIE-etched double mesa waveguides consisting in a 3 μm wide ridge (for lateral confinement of the guided modes) on top of a 100 μm wide mesa (to access the buried AlAs layers), with high propagation losses of $\sim 2\text{ cm}^{-1}$ in the near infrared, and a 3 $\%W^{-1}\text{cm}^{-2}$ normalized conversion efficiency [35]. This high attenuation coefficient was assumed to stem from

1. the poor quality of the etched sidewalls responsible for significant scattering losses and
2. long oxidation times (1h20min) during which the oxide quality was degraded.

After optimization of the design, dry etching has then been replaced with $\text{H}_2\text{SO}_4:\text{H}_2\text{O}_2:\text{H}_2\text{O}$ (3:1:1) chemical wet etching to obtain smoother sidewalls. The resulting losses of oxidized samples were reduced to $\sim 1.5\text{ cm}^{-1}$, and a normalized conversion efficiency of 1000 $\%W^{-1}\text{cm}^{-2}$ was estimated through SPDC around 2 μm [36]. Then, always in the same group, the waveguide geometry has been switched to single ridges ($3\mu\text{m} \times 3\mu\text{m}$) to shorten the oxidation time to several minutes, hence low losses of $\sim 0.7\text{ cm}^{-1}$ and a 1500 $\%W^{-1}\text{cm}^{-2}$ normalized conversion efficiency [10]. However, the slight etchant selectivity led to peculiar saw-tooth transverse profiles with mediocre process uniformity. Finally, sample homogeneity has been improved by using the non selective $\text{CH}_3\text{COOH}:\text{HBr}:\text{K}_2\text{Cr}_2\text{O}_7$ etchant (1:1:1) [37].

Two scanning electron microscopy images of finalized samples are presented in Figure 3. Despite the poor control on the waveguide transverse profile, chemical etching is still relevant compared to dry etching techniques such as ICP-RIE, whose development in terms of sidewalls roughness and chemical state is not yet satisfactory for low-loss integrated frequency converters [38].

Growth and processing

The epitaxial structures reported in Tables 1 and 2 have been grown on semi-insulating (001) GaAs substrates by means of molecular beam epitaxy (MBE). This technique enables the growth of high purity layers with a sharp control of their compositions and thicknesses, with abrupt interfaces. The former accuracy is important to meet the phase-matching condi-

tion at the desired wavelength, whereas the latter is essential to keep the scattering losses to a minimum.

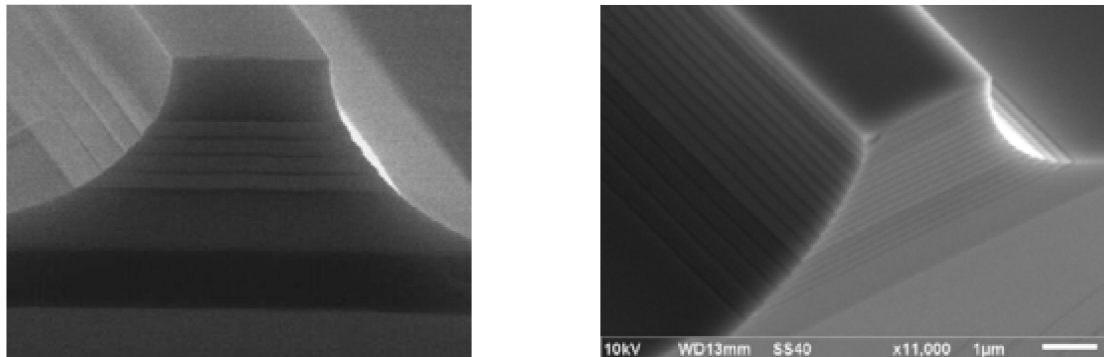


Figure 3. Scanning Electron Microscopy pictures of etched and oxidized waveguide facets (Left: “OPO Structure”– Right: “TTPS Structure”).

A thin film of positive photoresist is spin coated on the wafer and binary ridge patterns are defined with standard photolithography technique. Waveguides are oriented along the [110] crystalline direction in order to exploit the maximum $\chi^{(2)}_{xyz}$ element of the GaAs nonlinear susceptibility tensor and the {110} cleavage plane to define the waveguide facets. Typical $3\mu\text{m} \times 3\mu\text{m}$ ridges, are then etched using the $\text{CH}_3\text{COOH}:\text{HBr}:\text{K}_2\text{Cr}_2\text{O}_7$ solution. The resulting waveguide sidewalls are extremely smooth (roughness RMS value of 2 nm), which prevents the scattering of guided modes and favors the diffusion of the oxidant species during the oxidation step. The whole process is quite reproducible and easily homogeneous over several millimeters.

Samples are then cleaved in mm-long devices and the Al-rich layers are selectively oxidized. Oxidation is held in a quartz tube where samples are heated up to high temperatures in the 400°C - 500°C range, in a wet atmosphere. The latter is obtained using a 2L/min nitrogen flux flowing through a water bubbler stabilized at 70°C .

3.3. Optimization of the oxidation process

Optical propagation losses clearly originate from the oxidation process, for they are much lower before this fabrication step (respectively around 0.1 and 0.4 cm^{-1} in the near infrared for the best waveguides of the reported structures). Since the former demonstration of AlAs oxidation, such process has undergone a considerable progress in the last two decades, leading to reliable parameters for the kinetics of the reaction [34]. Thus, using the above mentioned processing technique and oxidation apparatus, this fabrication step has been carefully calibrated and optimized.

Furnace calibration

The kinetics of the oxidation depends on several parameters: the thickness and composition of the Al-rich layers, the furnace temperature, the carrier gas flux, and the bubbler tempera-

ture [33]. We have chosen here to focus only upon temperature, the carrier gas flux and the bubbler temperature being fixed to have an excess of reactants in the wet atmosphere. Figure 4 represents, for our grown AlAs layers, the log-log representation of lateral oxidation depth versus process duration, for different temperatures ranging from 400°C to 500°C. The linear progression of the oxide front with time is pointed out by the unitary slope of the dashed lines fitting the data, meaning that the process is reaction limited. From the y-intercept we can estimate the indicated oxidation rates, varying from fractions of microns to several microns per minute. Since the reaction is thermally-activated, they follow an Arrhenius law $r = r_0 \cdot \exp(-E_a/k_B T)$, where r is the oxidation rate (in $\mu\text{m}/\text{min}$), r_0 the reaction constant (in $\mu\text{m}/\text{min}$), E_a the activation energy (in eV), k_B the Boltzmann constant, and T the process temperature (in Kelvin). According to Figure 4 we obtain $E_a = 1.7\text{eV}$ in fair agreement with the literature [33].

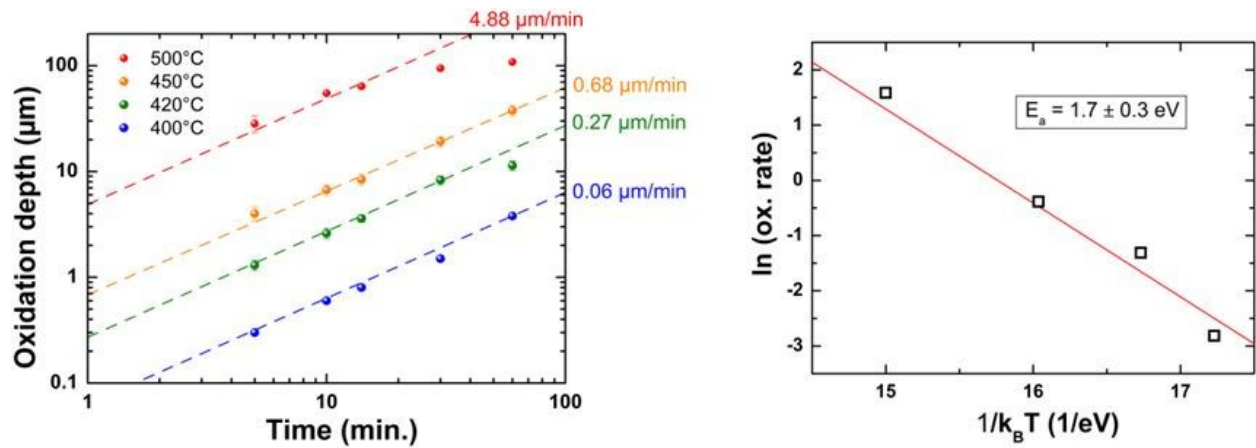


Figure 4. (Left) Lateral oxidation depth of 37.5nm thick $\text{Al}_{0.98}\text{Ga}_{0.02}\text{As}$ layers vs. Time, for several temperatures; (Right) Arrhenius plot of the oxidation rate.

Optimization of the oxidation parameters

Knowing the width of our ridge waveguides, the previous calibration allows us to estimate the nominal process duration required to complete the oxidation (*i.e.* when the oxidation fronts merge at the centre of the structure). Systematic loss measurements have been performed on several waveguides oxidized at 410°C, 420°C and 430°C, with oxidation durations around the estimated nominal values. In Figure 5 we report the average value and standard deviation of TE_{00} modal losses, conveniently measured around 1.55 μm . Data are normalized to the reference loss level obtained for a 14 minutes long oxidation at 420°C. Two conclusions can be drawn:

1. the average loss level suffers from slow oxidation kinetics, and
2. the process must be stopped at the exact moment when all the AlAs has been converted into oxide.

As we can see from the graph, this last condition is particularly difficult to meet at high temperature where losses are highly sensitive to any imprecision on the oxidation time. Consequently the set of parameters {14 min., 420°C} has been chosen as the best reasonable trade-off.

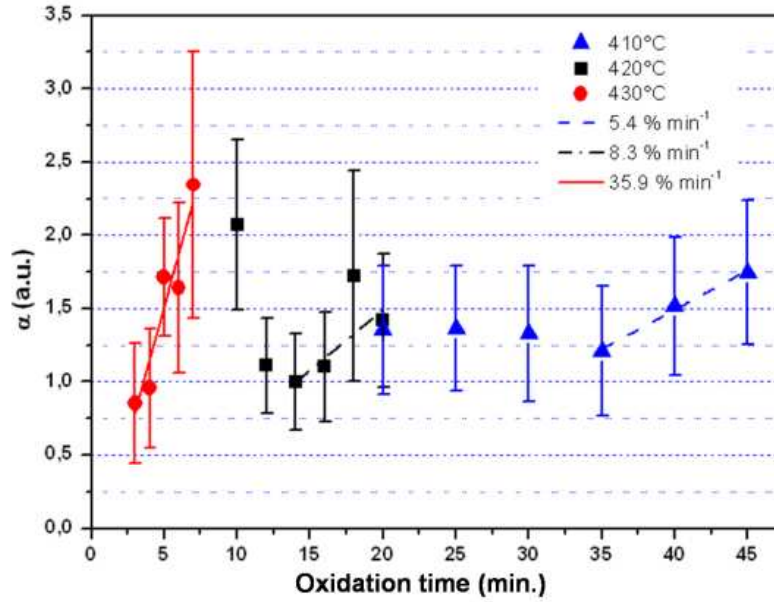


Figure 5. Normalized losses vs. Oxidation time for three different process temperatures.

4. Nonlinear optics experimental performances

4.1. Nonlinear optics characterization

Nonlinear characterization of a frequency converter is achieved through three-wave mixing experiments for which the nonlinearity of the material couples fields of angular frequency ω_i ($i=1,2,3$) such as $\omega_1+\omega_2=\omega_3$ [6]. Different setup configurations can be implemented depending on the modes injected at the guiding structure input, and several figures of merit can be inferred. Second harmonic generation ($\omega+\omega\rightarrow 2\omega$) is the simplest to achieve, as the output power of the generated beam scales quadratically with the input power. It enables the estimation of normalized conversion efficiency $\eta_{\text{norm}}=P_{2\omega}/(P_{\omega}^2L^2)$. The inverse process (at least at degeneracy) that is SPDC ($\omega_3\rightarrow\omega_1+\omega_2$) is more subtle to detect as the pump wave interacts with weak vacuum quantum fluctuations. It gives access to the device tuning curve and to the off-degeneracy conversion efficiency. Finally, seeded down-conversion ($\omega_3-\omega_1\rightarrow\omega_2$) can alternatively be described as DFG or parametric amplification. Normalized parametric gain $g/P^{1/2}=\eta_{\text{norm}}^{1/2}$ is crucial when it comes to optical parametric amplifiers (OPAs) and OPOs.

Since the first experimental demonstration of mid-infrared DFG in form birefringent waveguides in 1997 [35], the performances of such device have been significantly improved in terms of optical losses and conversion efficiency. Thereby, this phase-matching scheme has been successfully extended to visible and near infrared spectral ranges [9,10]. Concerning the first structure discussed here, designed for 1.06-to-2.12 μm parametric down-conversion, three-wave mixing experiments have been extensively carried out, and their results have already been published. A normalized conversion efficiency of $\eta_{\text{norm}} = 1500 \text{ \%W}^{-1}\text{cm}^{-2}$, corresponding to a normalized parametric gain of $3.9 \text{ cm}^{-1}\text{W}^{-1/2}$ at degeneracy, was estimated by parametric fluorescence measurements, and confirmed by SHG [10]. Direct parametric amplification measurements have been performed, and a maximum single-pass parametric gain of 4.5% has been obtained with 30 mW in-coupled pump power [37]. This the highest value ever reported in semiconductor waveguide. Furthermore, tunability for signal and idler beams in the 1.7 – 2.7 μm range has been established. The only limitation to this span was shown to stem from the O-H absorption band around 3 μm , due to the presence of hydroxide $\text{AlO}(\text{OH})$ [32]. Nevertheless, this band can be recovered, extending the tunability between 1.3 and 4.2 μm , after dehydroxylation of the sample (*i.e.* decomposing $\text{AlO}(\text{OH})$ into $\gamma\text{-Al}_2\text{O}_3$) by thermal annealing [39]. These main figures reflect the competitiveness of integrated GaAs-based frequency converter in the mid-infrared with respect to standard PPLN. However, the excessive propagation losses still prevent the use of cm-long waveguides in which the oscillation threshold would be at reach.

Shortly after the demonstration of SHG of a $\lambda = 1.6 \mu\text{m}$ pump in AlGaAs/AlOx waveguides as early as 1998 [40], the interest in the telecom band faded because of propagation loss issues. During the following decade, up and down-conversion between 0.775 μm and the telecom band remained out of reach for the form birefringent phase-matching scheme as the fabrication and oxidation steps were not fully optimized. In the following, we present our latest results obtained in the most recent generation of partially oxidized AlGaAs waveguides. State-of-the-art conversion efficiency is estimated *via* SHG experiment, and off-degeneracy dispersion is assessed by DFG experiment. A tunability greater than 500 nm is reported.

4.2. Second Harmonic Generation

In the experiment we report here, a CW single mode external cavity laser diode, largely tunable in the telecom band, was used to generate the pump beam at the fundamental frequency. The laser beam was TE-polarized then injected into a 500 μm long waveguide by end-fire coupling through a $\times 60$ (0.85 N.A.) microscope objective. The internal fundamental harmonic input power was estimated using the in-coupling efficiency of 37% assessed by taking into account the objective transmission (75%), the 28% facet reflectivity calculated accurately by finite-difference time domain (FDTD) method, and the overlap integral between the laser beam and the guided mode (69%). The second harmonic radiation was collected at the output facet by a similar microscope objective, filtered by a TM polarizer to get rid of the pump beam then focused onto a silicon photodiode connected to a lock-in amplifier.

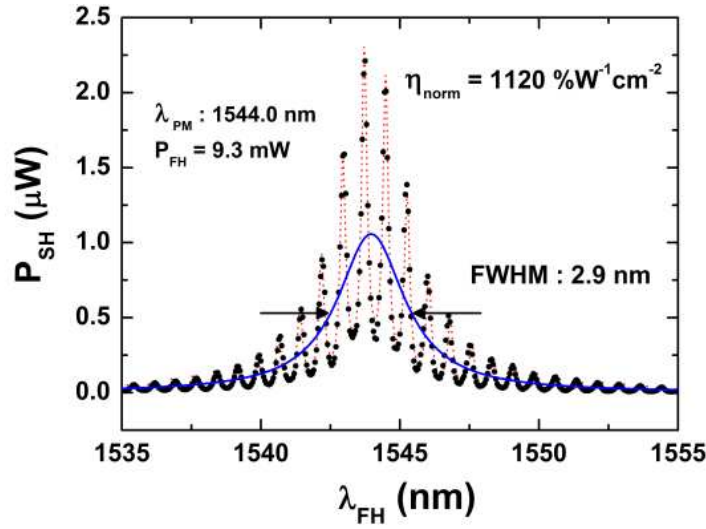


Figure 6. Second harmonic power vs. Fundamental harmonic wavelength. The photodiode signal (black dots) is theoretically fitted (red dotted line), and the Lorentzian single-pass phase-matching curve is extracted (solid blue line).

A typical phase-matching spectrum is shown in Figure 6. It was obtained by monitoring the second harmonic output power while scanning the fundamental harmonic input wavelength at constant 9.3 mW power. The experimental data exhibit a smooth phase-matching resonance modulated by Fabry-Perot fringes and can be nicely fitted after [41]. This high frequency feature corresponds to the interference pattern arising from the multiple reflections of the pump beam on the waveguide facets. Once the cavity fringes are filtered, the single-pass phase-matching curve is extracted and fitted by a Lorentzian curve with a 2.9 nm full width at half maximum (FWHM). The phase-matching condition is met at 1544 nm instead of the designed nominal value of 1550 nm. This slight discrepancy is a combined effect of the small systematic deviation of our MBE reactor on the layer thicknesses (typically 1 to 2 percents), the shift of the phase-matching wavelength induced by the 2D transverse confinement whereas the design procedure is 1D, and the temperature dependence of the structure refractive indices [42]. The broadening of the envelope shape and its deviation from the ideal *sinc* function are generally ascribed to waveguide inhomogeneities along propagation or to optical losses. In our case, however, the relatively large width and the high quality of the waveguide ridge suggest that we can assume waveguide invariance along propagation. Using the Fabry-Perot fringes method, TE optical losses, α_{FH} , were measured to be 0.4 cm⁻¹ and 1.2 cm⁻¹ in the 1.55 μm region, respectively before and after oxidation of the thin AlAs barriers. TM losses, α_{SH} , were assessed *via* transmission measurement of a Ti:Sapphire laser at 775 nm, yielding a value of 151 cm⁻¹. Consistently, losses of 140 cm⁻¹ were inferred for the second harmonic from the FWHM of the lorentzian curve according to the textbook equation [6]:

$$\eta \propto \exp\left[-(\alpha_{FH} + \alpha_{SH}/2)L\right] \times \frac{\sin^2(\Delta k L/2) + \sinh^2\left[(\alpha_{FH} - \alpha_{SH}/2)L/2\right]}{(\Delta k L/2)^2 + \left[(\alpha_{FH} - \alpha_{SH}/2)L/2\right]^2} \quad (1)$$

The evolution of the second harmonic power with the fundamental harmonic power at degeneracy is given in log-log scale in Figure 7. The quadratic law is confirmed by the slope of the line fitting the experimental data, and a SHG efficiency of $2.8 \%W^{-1}$ is estimated. The normalized conversion efficiency is found to be $1120 \%W^{-1}cm^{-2}$ *i.e.* comparable to the best value reported in AlGaAs waveguides [38], and which corresponds to a $3.3 cm^{-1}W^{-1/2}$ normalized parametric gain at degeneracy. Furthermore, no sublinear deviation is observed for pump power up to 50 mW, whereas such an onset occurs at 10 mW and is ascribed to two-photon absorption in [43]. Finally a maximum second harmonic power of 267 μW is reported, only limited by our source power at fundamental harmonic. This is the highest value reported for integrated AlGaAs waveguides.

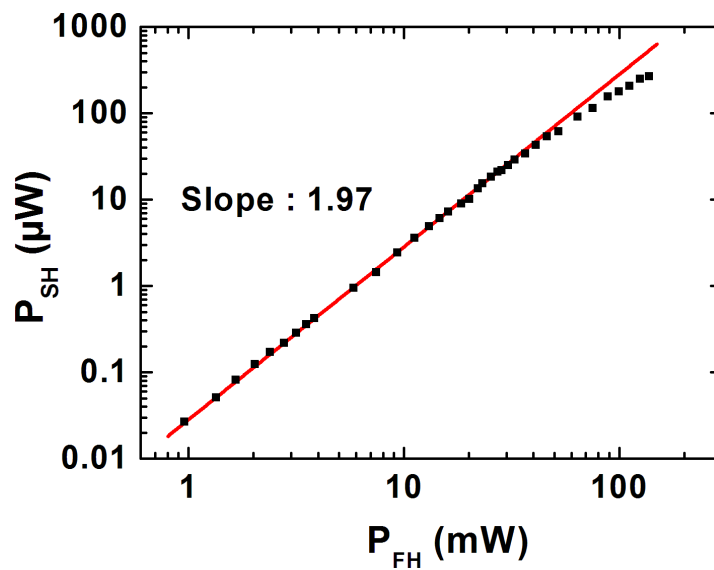


Figure 7. Log-log representation of second harmonic power vs. Fundamental harmonic power. The slope of the linear fit highlights the expected quadratic behavior.

4.3. Difference Frequency Generation

DFG was achieved on the same sample in order to investigate its performance out of degeneracy. In our case, this three-wave mixing process required a TM-polarized pump mode at visible wavelength λ_p , interacting with a TE-polarized infrared seed at wavelength λ_s , so to generate a TE-polarized difference frequency beam whose wavelength λ_{DF} is set by energy conservation $1/\lambda_{DF} = 1/\lambda_p - 1/\lambda_s$. The pump and seed beams were provided respectively by a linearly polarized CW Ti:Sapphire laser tunable around 775 nm, and an external cavity laser diode tunable between 1490 and 1600 nm. Both beams were combined using a 50/50 beam splitter then collinearly coupled in, and out of, a waveguide by two $\times 40$ (0.65 N.A.) microscope objectives. Its collimated output was either visualized on a camera or passed through a spectrometer before being filtered by a TE polarizer then detected using a strained InGaAs photodiode and a lock-in amplifier.

Typical spectra are shown in Figure 8, where the central peaks are unambiguously attributed to the second order of the residual pump beam diffracted by the monochromator grating. They were obtained for three different pump wavelengths below degeneracy ($\lambda_p = 773.2$ nm), after adjustment of the seed wavelength to optimize the difference frequency power. All the ($\lambda_p, \lambda_s, \lambda_{DF}$) sets verify energy conservation at phase-matching and are reported in Figure 9 along with the simulated tuning curve, with a good agreement. The spread of the dark line corresponds to the spectral acceptance of the DFG around phase-matching and its width accounts for the losses experienced by the three fields. Regarding the tunability of the device, we can see that a shift of the pump wavelength as small as 5.2 nm requires a spectral separation for the seed and difference frequency waves of 570 nm. This is due to the strong dispersion in the vicinity of material bandgap [44], and it turns out to be a great advantage regarding the fabrication of integrated source tunable in the near infrared for instance.

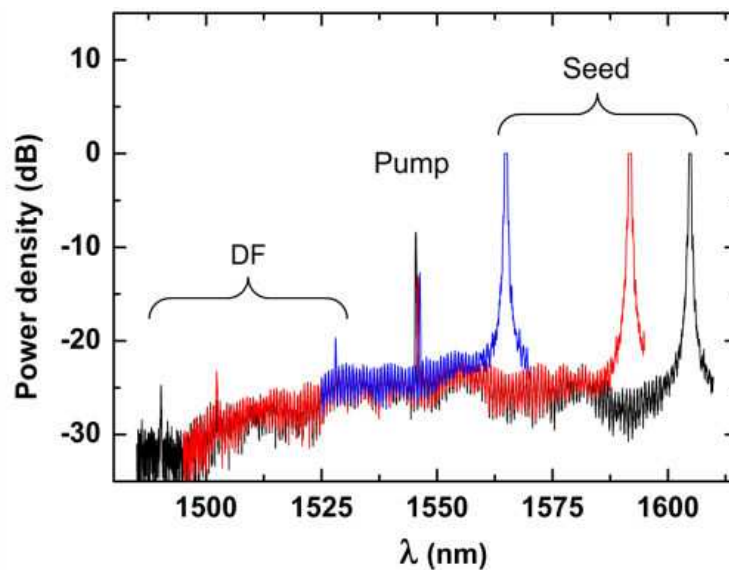


Figure 8. Normalized DFG spectra obtained for three different pump wavelengths (the seed peaks are clipped due to the lock-in finite dynamic range).

The combined study of SHG and DFG allowed us to fully characterize our form birefringent partially oxidized AlGaAs waveguides in terms of tunability and parametric gain. While this device strongly benefited from technologic improvements in terms of design, etching and oxidation, its performances compare favorably with respect to other alternative phase-matching approaches, but they are still limited by optical losses, which prevented so far the observation of SPDC. However, the reported figures are strongly motivating in view of the fabrication of a telecom source of quantum light. Indeed, for a 2 mm long waveguide, we theoretically estimate a parametric fluorescence efficiency of $\eta_{PF} \sim 1.7 \times 10^{-8}$ pairs/pump photon, whereas a significant reduction of optical losses to $\sim 1 \text{ cm}^{-1}$ would lead to $\eta_{PF} \sim 3 \times 10^{-7}$ pairs/pump photon, *i.e.* comparable with cm-long PPLN waveguides values [3].

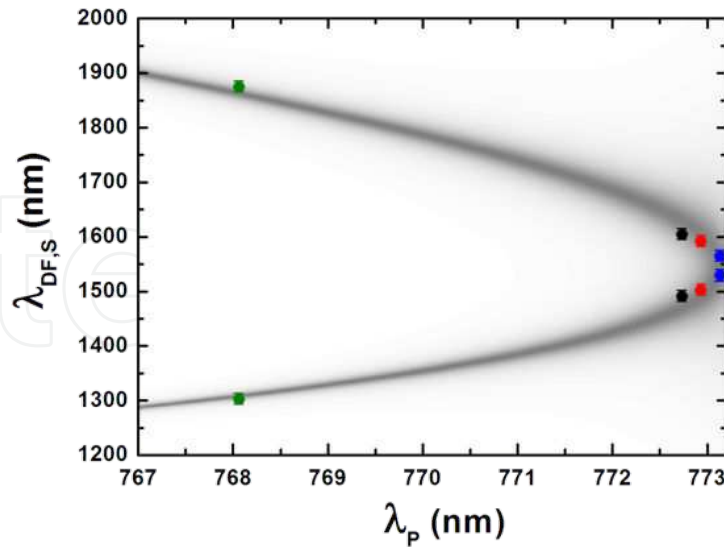


Figure 9. Tuning curve: experimental data (colored dots) and theoretical prediction (grayscale).

5. Phenomenological study of loss mechanisms

5.1. Structural and chemical characterization of the oxide

To date, the performances of partially oxidized AlGaAs waveguides are mitigated by high propagation losses ($\sim 1 \text{ cm}^{-1}$ in the infrared). As a comparison, typical PPLN waveguide losses are in the range of few 0.01 cm^{-1} , enabling the fabrication of several cm-long devices. Since optical propagation losses play a major role in all guided-wave phase-matching schemes proposed so far in the AlGaAs platform, their reduction is a critical issue.

Promising results have already been obtained by decreasing the losses after optimization of the waveguides design and the oxidation parameters, but today, a better understanding of the propagation losses origins is necessary if we want to lower them even more. Indeed, many aspects of the oxidation process are still not clearly established, including the exact formation mechanisms and the fine chemical and structural properties of the oxide. Therefore a transmission electron microscopy characterization of oxidized layers has been carried out [45] to assess the quality of the material at microscopic scale.

Chemical and structural characterization

The fabrication of cross-section samples has been carried out with an ion slicer used to perform the thinning of a waveguide oxidized guiding core. Based on high resolution transmission electron microscopy pictures combined with power spectrum analysis and energy filtered transmission electron microscopy images, it has been shown that:

- GaAs surrounding AlOx becomes amorphous in the close vicinity of the oxidized layers (~20 nm from the interface) and remains mono-crystalline beyond.
- Residual oxidation of the neighboring GaAs and $\text{Al}_{0.7}\text{Ga}_{0.3}\text{As}$ layers occurs through the interfaces, over 3 to 9 nm. The richer in aluminum the deeper an AlGaAs layer gets oxidized.
- The oxidation of $\text{Al}_{0.98}\text{Ga}_{0.02}\text{As}$ results in a 12% contraction of the layers thicknesses.
- AlOx layers are composed of $\gamma\text{-Al}_2\text{O}_3$ polycrystalline grains, with size between 10 and 20 nm, embedded in an amorphous AlOx matrix.

Interface roughness

Additionally, the internal interfaces were investigated by high-angle annular dark-field (HAADF) scanning transmission electron microscopy. Figure 10 shows two images of the same waveguide core area acquired before and after oxidation. Oxidation is obviously responsible for the deterioration of the multilayer morphology, as rough interfaces are clearly visible afterwards, especially at the bottom interface. The acquisition of several of such pictures contiguous over about 700 nm allowed us to reconstruct the respective roughness profiles. Gaussian fits of their autocorrelation functions have been performed in order to reliably extract their stochastic parameters: the RMS amplitude σ and the coherence length L_c . The results are summarized in Table 3 for the different types of interfaces.

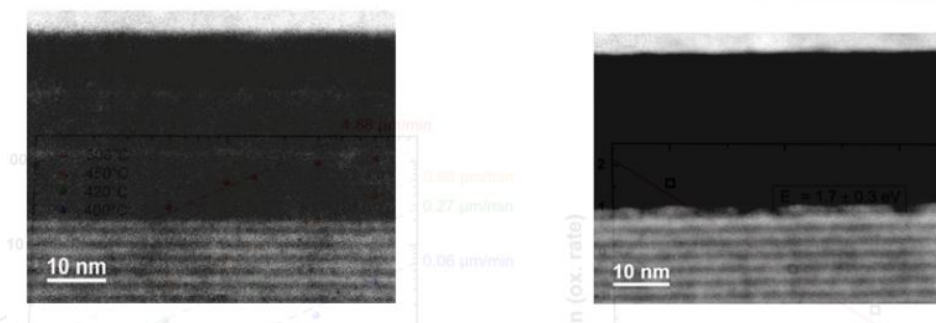


Figure 10. HAADF images of an $\text{Al}_{0.98}\text{Ga}_{0.02}\text{As}$ layer (in dark) embedded in GaAs (Top) and $\text{Al}_{0.7}\text{Ga}_{0.3}\text{As}$ (Bottom), before (Left) and after oxidation (Right).

Interface	GaAs/ $\text{Al}_{0.98}\text{Ga}_{0.02}\text{As}$	$\text{Al}_{0.7}\text{Ga}_{0.3}\text{As}/\text{Al}_{0.98}\text{Ga}_{0.02}\text{As}$	GaAs/AlOx	$\text{Al}_{0.7}\text{Ga}_{0.3}\text{As}/\text{AlOx}$
σ (nm)	0.37	0.37	0.53	0.69
$\Delta\sigma$ (nm)	0.08	0.08	0.08	0.06
L_c (nm)	4	4	53	30
ΔL_c (nm)	0	0	14	7

Table 3. Measured RMS amplitudes and coherence lengths for two types of interface, before and after oxidation.

For such step index waveguides with high index contrasts, optical modes are highly sensitive to any irregularities. We remind that the devices presented here are passive, and consequently the semiconductor alloys are chosen to be transparent for the wavelengths involved in the nonlinear process. Hence, assuming a good confinement by design, *i.e.* no substrate optical leakage, losses can only arise from scattering (rough sidewalls and layers interfaces, volume inhomogeneities) or absorption (defects).

Since the index contrast between AlOx and γ -Al₂O₃ is negligible, the polycrystalline grains are not expected to contribute significantly to scattering losses. Based on the previous observations, our work hypothesis was then to ascribe the optical propagation losses of the guided modes to scattering by the rough AlGaAs/AlOx boundaries.

5.2. Modeling the scattering by rough interfaces

The study of scattering losses in semiconductor waveguides is of great practical interest in the field of integrated optics, and since Marcuse's early work [46] a large amount of research has been done in this area. Most of the recent roughness studies in dielectric waveguides are now based on the convenient Lacey and Payne model [47,48], which offers the advantage to provide a semi-analytical expression for TE-mode losses, quite simply expressed in terms of fundamental waveguide parameters and statistics of the surface roughness.

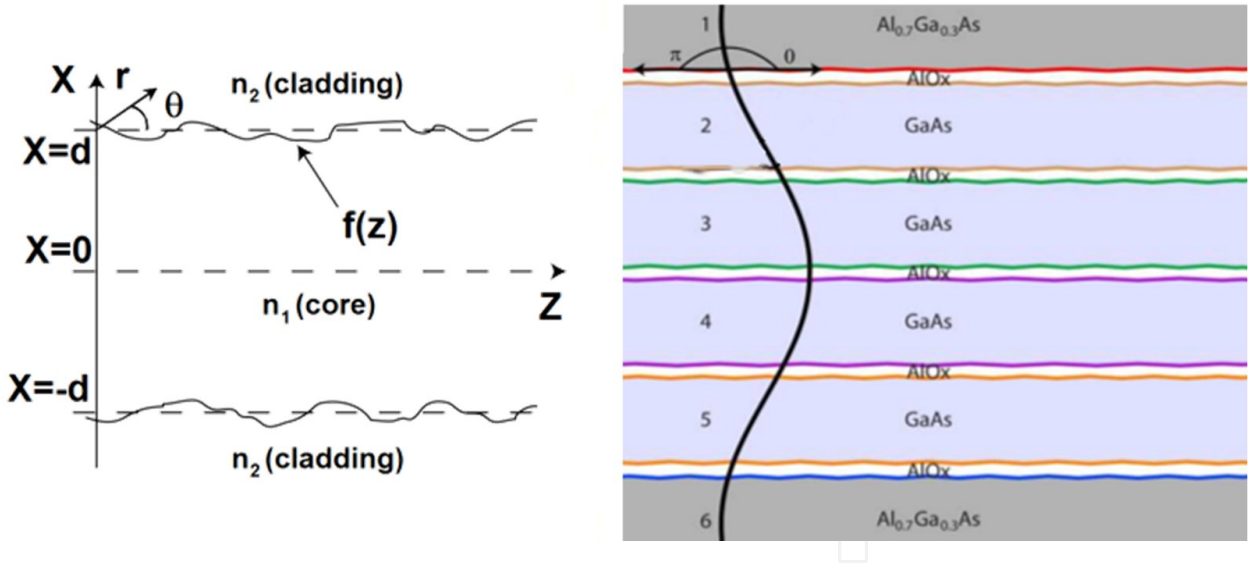


Figure 11. (Left) Schematics of rough interfaces in a slab waveguide. (Right) Schematics of the adaptation to our multilayer selectively oxidized waveguide.

The Lacey and Payne model deals with a three-layer slab core/cladding waveguide with rough interfaces as shown in Figure 11. It provides the scattering contribution to the propagation losses via the direct computation of the radiated far field, with the equivalent-current method [49]. Within this approach, it is possible to derive an expression for the exponential radiation loss coefficient due to scattering by the roughness, in a symmetric single mode waveguide of thickness $2d$:

$$\alpha_r = \phi^2(d) (n_1^2 - n_2^2)^2 \frac{k_0^3}{4\pi n_{eff}} \int_0^\pi \left[(1 + r(\theta))^2 + t(\theta)^2 \right] \tilde{R}(\beta - n_2 k_0 \cos(\theta)) d\theta \quad (2)$$

Where $\phi(d)$ is the modal field evaluated at the waveguide core/cladding interface, normalized following:

$$\int_{-\infty}^{+\infty} \phi^2(x) dx = 1 \quad (3)$$

n_1 and n_2 are the core and cladding refractive indices respectively, k_0 is the free-space wave vector, β is the modal propagation constant associated to the effective index n_{eff} , r and t are the respective reflection and transmission Fresnel coefficients and θ is the photon scattering angle with respect to the interface. The surface roughness of the waveguide walls is described by the spectral density function, which is obtained from the autocorrelation function $R(u)$ of the surface roughness via the Wiener-Khinchine theorem:

$$\tilde{R}(\Omega) = \int_{-\infty}^{+\infty} R(u) \exp(i\Omega u) du \quad (4)$$

This model requires two input parameters: the mean square deviation from a flat surface σ^2 and the correlation length L_c . The parameter σ^2 is related to the autocorrelation function by $R(0)=\sigma^2$, and the coherence length L_c of the interface profile corresponds to the half-width at half maximum of the Gaussian fit of the interface profile autocorrelation function.

To adapt this model to our multilayer structures, we ideally separate the waveguide in several microstructures. In Figure 11 we also show a scheme of one of our device, for which the interfaces are bunched in groups of two, in order to mark off regions with refractive index n_1 higher than the two adjacent ones n_2 . The core of each of these six microstructures, sandwiched between AlOx layers and bounded by rough interfaces, is identified and numbered from 1 to 6. Its refractive index is the one of the appropriate alloy (GaAs or $\text{Al}_{0.7}\text{Ga}_{0.3}\text{As}$).

In order to infer a rough estimate of the optical losses for the fundamental optical TE_0 mode, we compute α_i ($i=1,6$) the losses of each microstructure, then we simply convert the equation (2) under the assumption that each contribution adds up incoherently with the others:

$$\alpha_{tot} = \sum_{i=1}^6 \alpha_i \quad (5)$$

At this point, we should stress that our adaptation is very simplistic and its derivation is only qualitative.

5.3. Spectral study of propagation losses

Among the several different ways to measure optical losses, the Fabry-Perot fringes measurement is the most suitable technique for low-loss waveguides [50]. Unlike the cut-back method, it has the advantage of not being destructive, and contrary to transmission measurement, it is independent of coupling and collection efficiencies estimations. In this frame, we can picture the waveguide as a resonator in which guided modes are reflected by the cleaved facets and travel in both directions. By scanning the wavelength of the input wave, we observe a multiple wave interference pattern at the output, namely the Airy function of the cavity. The contrast and finesse of the resonances are straightforwardly linked to the number of waves participating to the total interference, therefore to the reflection (estimated by FDTD simulations) and propagation losses experienced by the traveling modes.

In order to test our hypothesis and investigate the optical loss mechanisms, we carried out a study on their spectral dependence. The results are reported in Figure 12, for both the structures presented previously. According to our phase-matching scheme, the data around λ_p represent the TM_{00} losses, whereas the data at wavelength close to degeneracy represent the TE_{00} losses.

The data were obtained by using external cavity diode lasers tunable in the telecom band from 1.3 to 1.6 μm , and a slightly tunable DFB laser around 2.12 μm . However we resorted to transmission measurements of a CW Ti:Sapphire laser around 1 μm and below, where losses were found to be too high to be reliably inferred from Fabry-Perot fringes.

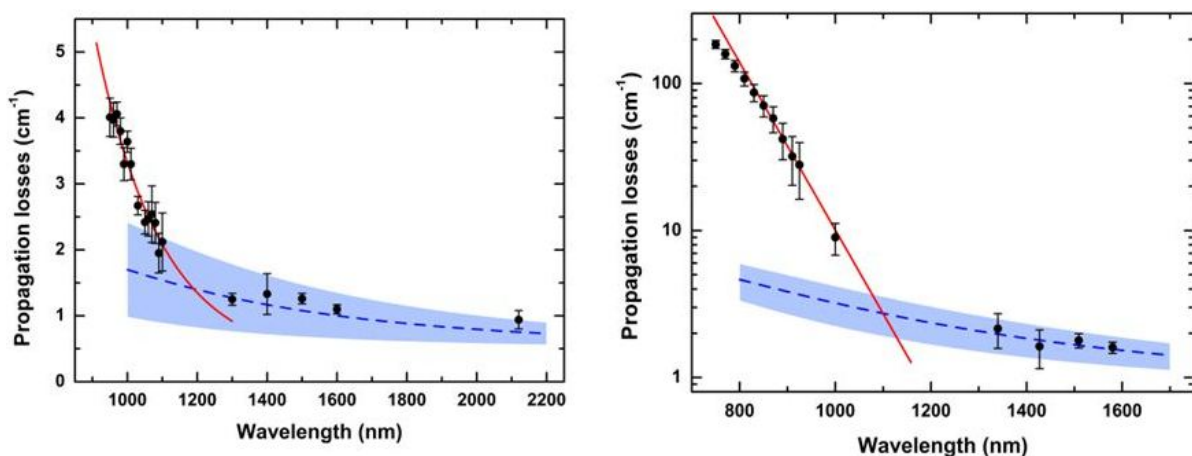


Figure 12. Propagation losses vs. Wavelength, fitted by decaying exponential (red curves) for short wavelengths, and inverse-power law (blue curves) for long wavelengths. The left (resp. right) figure corresponds to the OPO (resp. TTPS) structure.

Two different regimes are apparent: for wavelengths below $\sim 1.1 \mu\text{m}$, data are well fitted by decaying exponential curves (red lines), whereas their decays follow inverse power laws above $\sim 1.1 \mu\text{m}$.

For the longest wavelengths involved, losses are fairly low (around 1 cm^{-1} and less) and can be ascribed to the interfaces roughness that appears during oxidation. Indeed, the reasonable agreement between the experimental data (black dots) and the prediction band derived from our simple semi-analytical model (blue bands) confirms that, in this spectral range, losses are dominated by the scattering contribution in a Rayleigh-like regime. Note that this result is consistent with previous work achieved on an older generation of similar waveguides [51], in which losses were probed by scattered light measurements, and they were also found to decrease between 1.3 and $2.1\text{ }\mu\text{m}$.

For shorter wavelengths, our previous assumption is inadequate and a new loss mechanism must be considered. The very high losses and their exponential decay with wavelength suggest an Urbach's tail absorption, highlighting the fact that not only surface imperfections but also volume defects at the oxide interfaces play a critical role. As was already noticed several years ago [40], these additional losses are likely to be ascribed to arsenic antisites formed during oxidation at the oxide-semiconductor interface [52]. Trapped reaction products (*e.g.* elemental As and AsH_3) could explain this excess of arsenic and the resulting EL2-like crystalline defects, with donor levels in the gap of AlGaAs. Indeed, the transition between the two regimes occurs at photon energy corresponding to 65 to 70% of the bandgap of the waveguide core material (respectively GaAs and $\text{Al}_{0.25}\text{Ga}_{0.75}\text{As}$).

These levels of pump losses are currently the limiting factor for the efficiency of our AlGaAs integrated devices. Nevertheless, as shown by existing research on quantum-well luminescence close to oxidized layers [52] hydrogenation can be effectively used to remove absorbing species trapped at the oxide interfaces. Thermal annealing cycles are also expected to improve the crystallinity of spoiled materials. Moreover, a study on the spatial distribution of the mechanical strains arising from the volume shrinkage of oxidized thin AlAs layers showed that a critical overstrained zone appears at the merging point of the two counter-propagative oxidation fronts [53]. In our case, this could be an additional source of concern since the maximum intensity of the optical modes is at the confluence of the oxidation fronts. In order to circumvent such over-oxidation issue, new innovative designs are being tested (*e.g.* oxidation unidirectionally launched from one side of the ridge).

Despite the fact that propagation losses have prevented the use of form birefringent phase-matching scheme at its full potential, we are able to design and fabricate reasonably low-loss integrated waveguides. At the moment, aluminum oxide remains very promising for our photonic applications but its quality is not yet compatible with the most demanding nonlinear devices. Various investigations of its fine properties allowed us to better understand the loss mechanisms involved, and they gave us clues for their minimization. Improvement of the oxide quality is necessary for further significant progress, and will only occur after a specific technological development of the oxidation process, starting with the solutions evoked above which are currently under exploration.

6. Implementation of an integrated cavity

6.1. Design and fabrication of the cavity mirrors

A standard way to enhance nonlinear optical interactions consists in the insertion of the $\chi^{(2)}$ parametric gain medium into an optical resonator. The large amount of energy resulting from the light confinement inside the cavity enables to trigger nonlinear processes with lower input powers and larger efficiency. To this purpose, we have been focusing on the fabrication of an integrated resonant cavity. Indeed, regarding the realization of an OPO, the modest single-pass parametric gain in our waveguides makes the quality of the cavity mirrors critically important towards the reach of the oscillation threshold. One should stress that, in a 2 mm-long cavity, the mirror losses $\alpha_M = -\ln(R_1 R_2)/2L$ becomes of the order of the typical 1 cm^{-1} propagation losses as soon as their reflectivity reaches 82%.

As a trade-off between the pump power threshold and the spectral stability and tunability of the oscillator, we opted for a symmetric doubly resonant configuration (DROPO) with single pass of the pump, in which case the steady-state pump threshold at degeneracy P_p^{th} reads [54]:

$$P_p^{\text{th}} = \frac{1}{\eta_{\text{norm}}} \left(\frac{-\alpha_p \ln(R_{S,I} \exp(-\alpha_{S,I} L))}{2(1 - \exp(-\alpha_p L/2))} \right)^2 \quad (6)$$

With η_{norm} the waveguide normalized conversion efficiency, α_p the pump losses, $\alpha_{S,I}$ the signal and idler losses, L the waveguide length and $R_{S,I}$ the modal reflectivity at signal and idler wavelength. Consequently, for a 2 mm-long device, by plugging in our typical values of parametric gain and losses we can see that mirrors with reflectivity as high as 98.3% are required to have a threshold power of 100 mW, which is the maximum power that we can safely couple into the waveguide. The fabrication of such a demanding integrated cavity is all the more challenging that the adhesion of coating is made tricky, due to AlAs layers shrinkage during oxidation [55] producing non-ideal facets with possible irregular surface and mechanical stress. The high quality of the sample surface and waveguide sidewalls must also be preserved since the slightest deterioration would lead to additional scattering losses.

The solution we adopted to place our nonlinear waveguide in a DROPO resonator is the fabrication of integrated $\text{SiO}_2/\text{TiO}_2$ Bragg mirrors. The choice of these two materials has been dictated by the need to keep the thickness of the dielectric stack to a minimum thanks to their high-index contrast. The multilayer structures corresponding to the chosen cavity configuration are designed using commercial software [56] by implementing 1D transfer matrix algorithm along with optimization routines. They are then deposited by Ion beam Assisted Deposition (IAD) onto the cleaved facets of a sample, whose surface is protected from dielectric material overspray with a photoresist film lifted afterwards.

Figure 13a shows an experimental FTIR spectrum of a 6 bi-layers dielectric stack deposited on silicon substrate along with data acquired by focusing lasers with different wavelengths below a waveguide facet. The fair agreement between the experimental sets of data acquired on both the silicon and the sample substrates shows that the adhesion of the coating is satisfactory. The cleanliness of the sample surface can be appreciated on the scanning electron microscopy pictures provided in Figures 13b-c, where the dotted line highlights the edge of the waveguide.

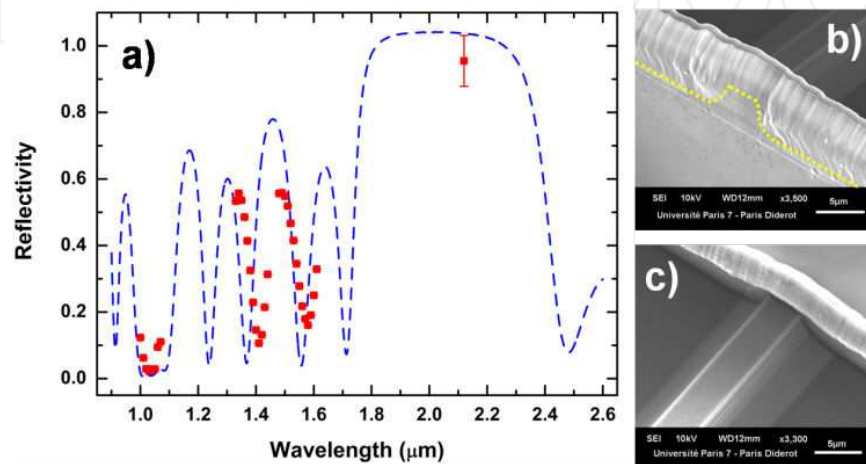


Figure 13. a) Experimental FTIR reflectivity spectrum of a cavity mirror, measured on a silicon substrate (dashed blue line) and below waveguide facet (red squares). b) and c) Bird's views of a mirror deposited on a waveguide facet.

6.2. Optical characterization

In order to quantitatively evaluate the coating optical quality, the modal reflectivity of the deposited mirrors was inferred from the study of the Fabry-Perot fringes. The Airy functions, presented in Figure 14 were acquired with a DFB laser diode slightly tunable around $2.12\ \mu\text{m}$ injected in a waveguide respectively without and with one coating. From the modification of the cavity finesse, increasing from 1.7 to 3.9, we can deduce a modal reflectivity of $\sim 85\%$ at this wavelength. The significant discrepancy from the designed nominal value of 98.5% can be explained by the simplicity of the design procedure that only considers plane waves perpendicularly impinging on an infinite surface mirror. Indeed, the effects of the guided-mode numerical aperture and the finite transverse dimensions of the mirror are not taken into account.

Finally, SPDC experiment has been achieved in those integrated cavities. The TM-polarized pump beam of a CW Ti:Sapphire laser, tunable around $1\ \mu\text{m}$, was injected through a $\times 60$ (0.85 N.A.) microscope objective into a 2-mm long waveguide with both facets coated. The device output was collected and collimated by an identical objective. Then it was passed through a germanium window to filter out the pump beam. Finally, the TE-polarized parametric fluorescence signal around $2\ \mu\text{m}$ was focused on a strained InGaAs photodiode and detected with a lock-in amplifier. In Figure 15 we have plotted the external signal power

measured after the exit mirror as a function of the external pump power focused onto the entrance mirror, while the pump wavelength was set at degeneracy. The nonlinear trend at high pump powers may be evidence that the nonlinear process tends to go beyond the low-gain regime. However, given the estimation of modal reflectivity, the oscillation threshold is currently out of reach. But beyond the demonstration of an integrated OPO, the scope of these technological results is very broad and could concern various types of integrated Al-GaAs-based nonlinear devices.

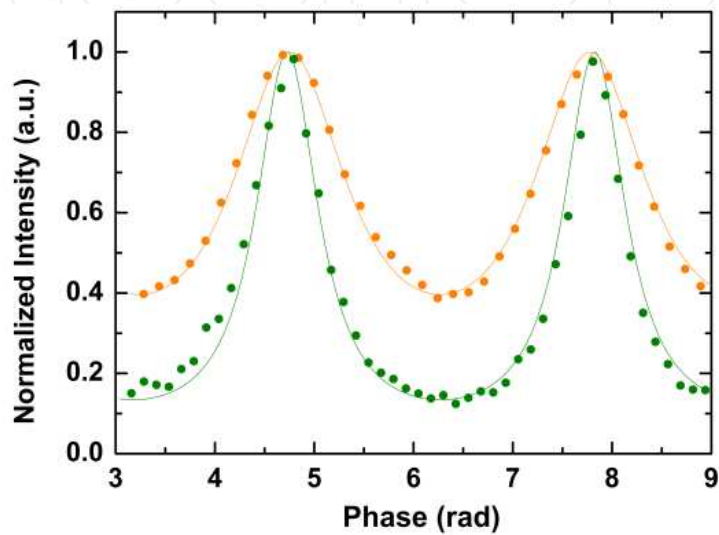


Figure 14. Fabry-Perot fringes of bare waveguide (orange) and semi-cavity (green) acquired around 2.12 μm .

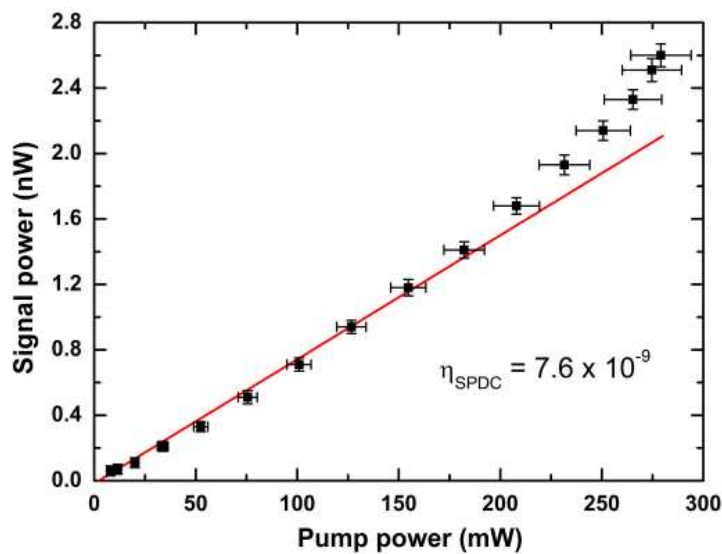


Figure 15. Generated output signal power vs. Input pump power (external values). The linear fit at low power (red solid line) points out the superlinear trend at high power.

7. Conclusion and perspectives

In this chapter we have shown that the field of semiconductor sources would largely benefit from the development of integrated AlGaAs nonlinear devices. Indeed, the demonstrations of an integrated OPO or a TTPS, for example, would have a great impact on applications such as optical spectroscopy and quantum telecommunications. The work presented in this chapter is part of the sustained research activity led on these two fronts.

Different technological solutions have been realized to fulfill the phase-matching condition necessary for efficient AlGaAs-based frequency converters. Thus it is interesting to compare their respective characteristics and performances.

It should first be noted that our “OPO structure”, designed for guided-wave parametric down-conversion of a 1.06 μm CW pump, cannot be straightforwardly be compared to any other AlGaAs device. Indeed, the closest existing research, which is on OP-GaAs OPOs, is not focusing at the moment on monolithic integration but rather on applications such as metrology or gas spectroscopy. Furthermore, because these setups have been operated in pulsed regime at first, the pump wavelength is fixed above 1.8 μm to avoid two-photon absorption in GaAs. Consequently, these crystals are optically pumped around 2 μm , and their degeneracy is typically between 4 and 5 μm .

The “TTPS structure” however is topical, as confirmed by the continuous track record of design and experimental results on 0.775-to-1.55 μm frequency conversion in semiconductor devices. An overview of the current state-of-the-art is given by Table 4, in which we reported the loss values, generated power, normalized conversion efficiency and spectral acceptance of type I CW SHG experiment for several phase-matching schemes. The figures in bold (resp. in italics) correspond to the best (resp. second best) value of each column.

This provides us with a synoptic vision of the strength and weakness of respectively modal phase-matching [57], QPM [24] and form birefringence phase-matching [9,38]. It is then quite clear that, regarding conversion efficiency, form birefringence phase-matching compare favorably with respect to modal phase-matching and QPM. Moreover, low infrared losses and high generated powers are enabled by optimized design and fabrication processes. The very high losses in the visible are caused by the presence of AlOx layers, and they are the current limiting factor of this phase-matching strategy. The resulting broadening of the $\chi^{(2)}$ process spectral acceptance may in turn be an issue for experimental protocols requiring spectrally narrow and pure sources of telecom twin-photons.

Ref.	$\alpha(1.55 \mu\text{m}) [\text{cm}^{-1}]$	$\alpha(775 \text{ nm}) [\text{cm}^{-1}]$	$P_{\text{SH}}[\mu\text{W}]$	$\eta_{\text{norm}}[\% \text{W}^{-1} \text{cm}^{-2}]$	$\Delta\lambda [\text{nm}]$
[57]	7.8	41	0.023	6.8×10^{-3}	0.9
[24]	1.7	2.2	6.6	92	0.3
[38]	5.3	70	10^{-4}	1250	10
[9]	1.1	140	267	1120	3

Table 4. Summarize of the characteristics and performances of devices implementing different phase-matching schemes.

In conclusion, we have shown that, although the choice of AlGaAs/AlOx nonlinear waveguides is relevant to fabricate highly efficient integrated frequency converters, losses remain the main bottleneck and prevent further breakthrough. Nevertheless, progress has been made by investigating the different loss mechanisms, and a specific technological development of the AlAs oxidation process is expected to reduce further optical losses. Finally, we have demonstrated the feasibility of monolithic integrated Fabry-Perot cavity, by depositing highly reflective dielectric mirrors on the waveguide facets.

Acknowledgements

The authors warmly acknowledge Alessio Andronico for help in the simulations, and Guilhem Almuneau for experimental help.

Author details

M. Savanier¹, C. Ozanam¹, F. Ghiglieno¹, L. Lanco², X. Lafosse², A. Lemaître², I. Favero¹, S. Ducci¹ and G. Leo¹

1 Université Paris Diderot, Sorbonne Paris Cité, Laboratoire Matériaux et Phénomènes Quantiques, CNRS-UMR 7162, France

2 Laboratoire de Photonique et de Nanostructures, CNRS-UPR 20, France

References

- [1] Langrock, C., Kumar, S., Mc Geehan, J. E., Willner, A. E., & Fejer, M. M. (2006). All-optical signal processing using $\chi^{(2)}$ nonlinearities in guided-wave devices. *IEEE Journal of Lightwave Technology*, 24(7), 2579.
- [2] Werle, P. (1998). A review of recent advances in semiconductor laser based gas monitors. *Spectrochimica Acta Part A: Molecular and Biomolecular Spectroscopy*, 54(2), 197.
- [3] Tanzilli, S., Tittel, W., De Riedmatten, H., Zbinden, H., Baldi, P., De Micheli, M., Ostrowsky, D. B., & Gisin, N. (2002). PPLN waveguide for quantum communication. *The European Physical Journal D Atomic, Molecular, Optical and Plasma Physics*, 18(2), 155.
- [4] Pavesi, L. (2003). Will silicon be the photonic material of the third millennium? *Journal of Physics: Condensed Matter*, 15(26), R1169.

- [5] Roelkens, G., Liu, L., Liang, D., Jones, R., Fang, A., Koch, B., & Bowers, J. (2010). III-V/silicon photonics for on-chip and intra-chip optical interconnects. *Laser & Photonics Reviews*, 4(6), 751.
- [6] Sutherland, R. L. (2003). Handbook of nonlinear optics. *New York: Marcel Dekker*.
- [7] Lanco, L., Ducci, S., Likforman, J. P., Marcadet, X., van Houwelingen, J. A. W., Zbinden, H., Leo, G., & Berger, V. (2006). A semiconductor waveguide source of counter-propagating twin photons. *Physical Review Letters*, 97(17), 173901.
- [8] Horn, R., Abolghasem, P., Bijlani, B. J., Kang, D., Helmy, A. S., & Weihs, G. (2012). Monolithic source of photon pairs. *Physical Review Letters*, 108(15), 153605.
- [9] Savanier, M., Andronico, A., Lemaître, A., Galopin, E., Manquest, C., Favero, I., Ducci, S., & Leo, G. (2011). Large second-harmonic generation at 1.55 μm in oxidized Al-GaAs waveguides. *Optics Letters*, 36(15), 2955.
- [10] Ravaro, M., Le Dû, M., Likforman, J. P., Ducci, S., Berger, V., Marcadet, X., & Leo, G. (2007). Estimation of parametric gain in GaAs/AlOx waveguides by fluorescence and second harmonic generation measurements. *Applied Physics Letters*, 91(19), 191110.
- [11] Siegman, A. E. (1986). Lasers, Mill Valley, Calif. *University Science Books*.
- [12] Hall, R. N., Fenner, G. E., Kingsley, J. D., Soltys, T. J., & Carlson, R. O. (1962). Coherent light emission from GaAs junctions. *Physical Review Letters*, 9(9), 366.
- [13] Faist, J., Capasso, F., Sivco, D. L., Sirtori, C., Hutchinson, A. L., & Cho, A. Y. (1994). Quantum cascade laser. *Science*, 264(5158), 553.
- [14] Lehnhardt, T., Hümmer, M., Rößner, K., Müller, M., Höfling, S., & Forchel, A. (2008). Continuous wave single mode operation of GaInAsSb/GaSb quantum well lasers emitting beyond 3 μm . *Applied Physics Letters*, 92(18), 183508.
- [15] Laffaille, P., Moreno, J. C., Teissier, R., Bahriz, M., & Baranov, A. N. (2012). High temperature operation of short wavelength InAs-based quantum cascade lasers. *AIP Advances*, 2(2), 022119.
- [16] Feng, X., Caneau, C., Le Blanc, H. P., Visovsky, N. J., Chaparala, S. C., Deichmann, O. D., Hughes, L. C., Chung-en, Z., Caffey, D. P., & Day, T. (2011). Room temperature CW operation of short wavelength quantum cascade lasers made of strain balanced $\text{Ga}_x\text{In}_{1-x}\text{As}/\text{Al}_y\text{In}_{1-y}\text{As}$ material on InP substrates. *IEEE Journal of Selected Topics in Quantum Electronics*, 17(5), 1445.
- [17] The Scott Partnership. (2010). Mid-infrared lasers. *Nature Photonics*, 4(8), 576.
- [18] Vizbaras, A., Anders, M., Katz, S., Grasse, C., Boehm, G., Meyer, R., Belkin, M. A., & Amann, M. C. (2011). Room-temperature $\lambda \approx 2.7 \mu\text{m}$ quantum cascade laser sources based on intracavity second-harmonic generation. *IEEE Journal of Quantum Electronics*, 47(5), 691.

- [19] Salter, C. L., Stevenson, R. M., Farrer, I., Nicoll, C. A., Ritchie, D. A., & Shields, A. J. (2010). An entangled-light emitting diode. *Nature*, 465(7298), 594.
- [20] Parameswaran, K. R., Route, R. K., Kurz, J. R., Roussev, R. V., Fujimura, M., & Fejer, M. M. (2002). Highly efficient second-harmonic generation in buried waveguides formed by annealed and reverse proton exchange in periodically poled lithium niobate. *Optics Letters*, 27(3), 179.
- [21] Pomarico, E., Sanguinetti, B., Gisin, N., Thew, R., Zbinden, H., Schreiber, G., Thomas, A., & Sohler, W. (2009). Waveguide-based OPO source of entangled photon pairs. *New Journal of Physics*, 11(11), 113042.
- [22] Orlov, S., Grundkötter, W., Hofmann, D., Quiring, V., Ricken, R., Suche, H., & Sohler, W. (2008). Mid-infrared integrated optical parametric generators and oscillators with periodically poled Ti:LiNbO₃ waveguides. *Ebrahimzadeh M., Sorokina I. T. (eds.) Mid-Infrared Coherent Sources and Applications. Dordrecht, The Netherlands: Springer*, 377.
- [23] Stegeman, G. I., Villeneuve, A., Kang, J., Aitchison, J. S., Ironside, C. N., Al-Hemyari, K., Yang, C. C., Lin, C., , H., Lin, H., , H., Kennedy, G. T., Grant, R. S., & Sibbett, W. (1994). AlGaAs below half bandgap: the silicon of nonlinear optical materials. *Journal of Nonlinear Optical Physics & Materials*, 3(3), 347.
- [24] Yu, X., Scaccabarozzi, L., Lin, A. C., Fejer, M. M., & Harris, J. S. (2007). Growth of GaAs with orientation-patterned structures for nonlinear optics. *Journal of Crystal Growth*, 301(1), 163.
- [25] Vodopyanov, K. L., Levi, O., Kuo, P. S., Pinguet, T. J., Harris, J. S., Fejer, M. M., Gerard, B., Becouarn, L., & Lallier, E. (2004). Optical parametric oscillation in quasi-phase matched GaAs. *Optics Letters*, 29(16), 1912.
- [26] Fiore, A., Berger, V., Rosencher, E., Bravetti, P., & Nagle, J. (1998). Phase-matching using an isotropic nonlinear material. *Nature*, 391(6666), 463.
- [27] Van der Ziel, J. P. (1975). Phase-matched harmonic generation in a laminar structure with wave propagation in the plane of the layers. *Applied Physics Letters*, 26(2), 60.
- [28] Dallesasse, J. M., Holonyak, N., Sugg, A. R., Richard, T. A., & El -Zein, N. (1990). Hydrolyzation oxidation of Al_xGa_{1-x}As-AlAs-GaAs quantum-well heterostructures and superlattices. *Applied Physics Letters*, 57(26), 2844.
- [29] Chen, E. I., Holonyak Jr, N., & Maranowski, S. A. (1995). Al_xGa_{1-x}As-GaAs metal-oxide semiconductor field effect transistors formed by lateral water vapor oxidation of AlAs. *Applied Physics Letters*, 66(20), 2688.
- [30] Mac, Dougal. M. H., Dapkus, P. D., Pudikov, V., Zhao, H., & Yang, G. M. (1995). Ultralow threshold current vertical-cavity surface-emitting lasers with AlAs oxide-GaAs distributed Bragg reflectors. *IEEE Photonics Technology Letters*, 7(3), 229.
- [31] Huffaker, D. L., Deppe, D. G., Kumar, K., & Rogers, T. J. (1994). Native oxide defined ring contact for low threshold vertical cavity lasers. *Applied Physics Letters*, 65(1), 97.

- [32] Bravetti, P., Fiore, A., Berger, V., Rosencher, E., & Nagle, J. (1998). 5.2-5.6 μm source tunable by frequency conversion in a GaAs-based waveguide. *Optics Letters*, 23(5), 331.
- [33] Choquette, K. D., Geib, K. M., Ashby, C. I. H., Twesten, R. D., Blum, O., Hou, H. Q., Follstaedt, D. M., Eugene, Hammons. B., Mathes, D., & Hull, R. (1997). Advances in selective wet oxidation of AlGaAs alloys. *IEEE Journal of Selected Topics in Quantum Electronics*, 3(3), 916.
- [34] Suárez, I., Almuneau, G., Condé, M., Arnoult, A., & Fontaine, C. (2009). Optimal control of AlAs oxidation via digital alloy heterostructure compositions. *Journal of Physics D: Applied Physics*, 42(17), 175105.
- [35] Fiore, A., Berger, V., Rosencher, E., Bravetti, P., Laurent, N., & Nagle, J. (1997). Phase-matched mid-infrared difference frequency generation in GaAs-based waveguides. *Applied Physics Letters*, 71(25), 3622.
- [36] De Rossi, A., Berger, V., Calligaro, M., Leo, G., Ortiz, V., & Marcadet, X. (2001). Parametric fluorescence in oxidized aluminum gallium arsenide waveguides. *Applied Physics Letters*, 79(23), 3758.
- [37] Guillotel, E., Ravaro, M., Ghiglieno, F., Langlois, C., Ricolleau, C., Ducci, S., Favero, I., & Leo, G. (2009). Parametric amplification in GaAs/AlOx waveguide. *Applied Physics Letters*, 94(17), 171110.
- [38] Scaccabarozzi, L., Fejer, M. M., Huo, Y., Fan, S., Yu, X., & Harris, J. S. (2006). Enhanced second-harmonic generation in AlGaAs/Al_xO_y tightly confining waveguides and resonant cavities. *Optics Letters*, 31(24), 3626.
- [39] Ravaro, M., Guillotel, E., Le Dû, M., Manquest, C., Marcadet, X., Ducci, S., Berger, V., & Leo, G. (2008). Nonlinear measurement of mid-infrared absorption in AlOx waveguides. *Applied Physics Letters*, 92(15), 151111.
- [40] Fiore, A., Janz, S., Delobel, L., van der Meer, P., Bravetti, P., Berger, V., Rosencher, E., & Nagle, J. (1998). Second-harmonic generation at $\lambda \sim 1.6 \mu\text{m}$ in AlGaAs/Al₂O₃ waveguides using birefringence phase matching. *Applied Physics Letters*, 72(23), 2942.
- [41] Ota, J., Narita, W., Ohta, I., Matsushita, T., & Kondo, T. (2009). Fabrication of periodically-inverted AlGaAs waveguides for quasi-phase-matched wavelength conversion at 1.55 μm . *Japanese Journal of Applied Physics*, 48(4), 04C110.
- [42] Gehrsitz, S., Reinhart, F. K., Gourgon, C., Herres, N., Vonlanthen, A., & Sigg, H. (2000). The refractive index of Al_xGa_{1-x}As below the band gap: Accurate determination and empirical modelling. *Journal of Applied Physics*, 87(11), 7825.
- [43] Abolghasem, P., Han, J., Bijlani, B. J., Arjmand, A., & Helmy, A. S. (2009). Highly efficient second-harmonic generation in monolithic matching layer enhanced Al_xGa_{1-x}As Bragg reflection waveguides. *IEEE Photonics Technology Letters*, 21(19), 1462.

- [44] De Rossi, A., Berger, V., Leo, G., & Assanto, G. (2005). Form birefringence phase-matching in multilayer semiconductor waveguides: tuning and tolerances. *IEEE Journal of Quantum Electronics*, 41(10), 1293.
- [45] Guillotel, E., Langlois, C., Ghiglieno, F., Leo, G., & Ricolleau, C. (2010). TEM characterization of oxidized AlGaAs/AlAs nonlinear optical waveguides. *Journal of Physics D: Applied Physics*, 43(38), 385302.
- [46] Marcuse, D. (1969). Mode conversion caused by surface imperfections of a dielectric slab waveguide. *Bell System Technical Journal*, 48(10), 3197.
- [47] Lacey, J. P. R., & Payne, F. P. (1990). Radiation loss from planar waveguides with random wall imperfections. *IEE Proceedings Optoelectronics*, 137(4), 282.
- [48] Schmid, J. H., Del  ge, A., Lamontagne, B., Lapointe, J., Janz, S., Cheben, P., Den-smore, A., Waldron, P., Xu, D. X., & Yap, K. P. (2008). Interference effect in scattering loss of high-index contrast planar waveguides caused by boundary reflections. *Optics Letters*, 33(13), 1479.
- [49] Snyder, A. W., & Love, J. D. (1983). Optical waveguide theory. London: Chapman and Hall.
- [50] De Rossi, A., Ortiz, V., Calligaro, M., Lanco, L., Ducci, S., Berger, V., & Sagnes, I. (2005). Measuring propagation loss in a multimode semiconductor waveguide. *Journal of Applied Physics*, 97(7), 073105.
- [51] Rao, S. V., Moutzouris, K., Ebrahimzadeh, M., De Rossi, A., Gintz, G., Calligaro, M., Ortiz, V., & Berger, V. (2003). Influence of scattering and two-photon absorption on the optical loss in GaAs/Al₂O₃ nonlinear waveguides measured using femtosecond pulses. *IEEE Journal of Quantum Electronics*, 39(3), 478.
- [52] Shi, S. S., Hu, E. L., Zhang, J. P., Chang, Y. L., Parikh, P., & Mishra, U. (1997). Photoluminescence study of hydrogenated aluminum oxide-semiconductor interface. *Applied Physics Letters*, 70(10), 1293.
- [53] Chouchane, F., Almuneau, G., Gauthier-Lafaye, O., Monmayrant, A., Arnoult, A., Lacoste, G., & Fontaine, C. (2011). Observation of overstrain in the coalescence zone of AlAs/AlOx oxidation fronts. *Applied Physics Letters*, 98(26), 261921.
- [54] Bava, G., Montrosset, I., Sohler, W., & Suche, H. (1987). Numerical modeling of Ti:LiNbO₃ integrated optical parametric oscillators. *IEEE Journal of Quantum Electronics*, 23(1), 42.
- [55] Durand, O., Wyckzisk, F., Olivier, J., Magis, M., Galtier, P., De Rossi, A., Calligaro, M., Ortiz, V., Leo, G., & Assanto, G. (2003). Contraction of aluminum oxide thin layers in optical heterostructures. *Applied Physics Letters*, 83(13), 2554.
- [56] Thin film center Inc. Essential MacLeod. <http://www.thinfilmcenter.com/essential.html>.

- [57] Abolghasem, P., Han, J., Bijlani, B. J., Arjmand, A., & Helmy, A. S. (2009). Continuous-wave second harmonic generation in Bragg reflection waveguides. *Optics Express*, 17(11), 9460.

IntechOpen

IntechOpen

